Modeling of aerodynamic disturbances for proximity flight of multirotors

Karan P. Jain[1], Trey Fortmuller[1], Jaeseung Byun[1], Simo A. Mäkiharju[2], and Mark W. Mueller[1]

***Abstract*— This paper presents a model to predict aerodynamic disturbances during close formation flight of two multirotors. The model is based on a propeller velocity field model and characterization of change in propeller thrust under oncoming flow. Using this model, we predict forces and torques on one mutirotor due to downwash of the other with respect to relative separation of the multirotors. We conduct proximity flight experiments using two types of quadcopters to measure forces and torques using accelerometer and rate-gyro. Predictions from the model and results from experiments match well for vertical separations greater than seven times the vehicle size. This verifies the range of fidelity of the model.**

I. Introduction

The maneuverability and agility that multirotors offer lends these vehicles to applications such as mapping, inspection, surveillance, and delivery. They are often utilized as cooperative aerial vehicles, for instance in the case of multi-agent construction tasks [1], [2] and observing moving targets [3], [4]. In all these contexts, some of the biggest limitations of multirotors are their limited endurance, range, and payload capacity.

Having the capability to swap batteries, change sensor suites, or hand off packages from one vehicle to another in mid-air would represent an improvement in vehicle performance with minimal interruption to a mission. Accomplishing any of these tasks necessitates the ability to dock two vehicles in flight, or at least operate in proximity. An important consideration for rigidly docking two vehicles is the mutual aerodynamic interference experienced by each vehicle flying in proximity during a docking maneuver.

Current literature covers various aspects of aerodynamic performance of multirotors. Aerodynamic influences on control of these vehicles have been studied, including ground effect [5] and ceiling effect for bridge inspection [6]. The effect on flight performance due to the downwash of a neighboring vehicle is of prime importance for flying multiple vehicles in proximity. One approach to address these disturbances is to constrain the trajectories of the vehicles to avoid downwash from the vehicles above, either completely or partially. For example, [7] experimentally measured wind velocities below a multirotor to observe the distance where the downwash effect is negligible, and [8] uses obstacle avoidance to prevent downwash interference. Having a model for the forces and torques experienced by a vehicle in downwash could allow for the development of controllers robust to these disturbances. This would allow for relaxation of some constraints on planning vehicles' trajectories amongst neighboring vehicles, such as in a swarm.

We present a model to analyze the aerodynamic forces and torques that multirotors experience during proximity flights. We use results from a UAV downwash model [9] and a propeller slipstream model [10] to develop some intuition and visualize the downwash below a quadcopter. We combine ideas from these models with our experimental data to create a spatial velocity field map below a multirotor. Lastly, we characterize the change in thrust produced by each propeller of a vehicle when subjected to oncoming flows from above. The theoretical velocity map combined with the change in propeller thrust is then used to estimate disturbances on a multirotor flying at a relative separation from another.

We then present an experimental analysis of experienced aerodynamic disturbances during close formation flight of two multirotors. Figure 1 shows the two types of quadcopters that are used in our experiments, a large quadcopter and a small quadcopter. The specifications of these vehicles are given in Table I. Vehicles on the scale of the large quadcopter have sufficient payload capacity to carry useful sensors such as cameras, gimbals, or LIDARs and are thus widely used. The scale of the small quadcopter was chosen to have a payload capacity similar to the weight of a large quadcopter's battery, allowing for future work in swapping batteries mid-flight. This could enable minimally interrupted flight strategies where, for example, the large quadcopter can perform tasks such as surveillance and the small quadcopter can replace a discharged battery of the large quadcopter with a charged one.

In our experiments, the two vehicles are flown simultaneously with various horizontal and vertical separations. We record the vehicles' instantaneous accelerations and angular velocities using an on-board inertial measurement unit (IMU) in the domain of aerodynamic interference. We also record the instantaneous position and orientation of the vehicles using a motion-capture system. These measurements are used to estimate aerodynamic force and torque as a function of relative separation of the vehicles. We compare our results with predictions from our model to validate the model for our task.

This paper is organized as follows: Section II presents a model for predicting disturbances on multirotors flying in proximity, Section III derives the equations for obtaining these disturbances experimentally using IMU data, and Section IV shows our laboratory setup, model predictions, experimental results, and validation of the model.

The authors are with [1]High Performance Robotics Lab and [2]FLOW Lab, Mech. Eng. Dept., University of California, Berkeley, CA 94720, USA. {karanjain, tfortmuller, jaeseungbyun, makiharju, mwm}@berkeley.edu

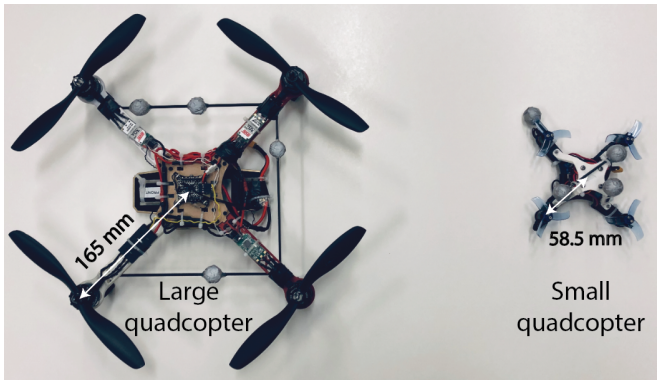

Fig. 1: The large quadcopter and small quadcopter used in the experiments

TABLE I: Physical parameters of test vehicles

Parameter (symbols)	Small quadcopter	Large quadcopter
Propeller diameter (D_p)	50.8 mm	203.2 mm
Arm length (l)	58.5 mm	165.0 mm
Mass (m)	145 g	650 g
Maximum thrust ($\mathrm{T_{max}}$)	4.6 N	27 N

II. Aerodynamic Interference Model

We assume that the aerodynamic disturbances experienced by a multirotor flown in the downwash of another multirotor are primarily the result of two mechanisms:

1) Drag from oncoming flow on the frame of the vehicle
2) Change in propeller thrust due to oncoming flow

The oncoming flow is due to the downwash of a multirotor. Hence, both mechanisms require a knowledge of the velocity field produced below a multirotor. Subsection II-A explains the velocity field model that we employ. The mechanisms are elaborated upon in subsections II-B and II-C.

A. Velocity field model

We apply the following assumption on multirotor downwash flow field based on [9]: cross-stream flow is negligible. Axial velocity, which is along $\boldsymbol{z}_B$ (the unit vector along z-axis of the concerned body), is the major component of the velocity field, and the only component we deal with.

The propeller slipstream model [10] provides an expression for the velocity field below a single propeller. It assumes that the flow is established three propeller diameters down the flow.

We model the flow field in the zone of established flow (ZEF) as axisymmetric. The velocity is now a function of vertical (axial) and horizontal (radial) separation, z and r respectively. Note that for a propeller's ZEF, low velocity induced at the center of a propeller disappears, which enables us to apply the Gaussian profile approximation with respect to radial separation [11]. Based on this information, we assume that for a multirotor's ZEF ($z > 3L$), the flows from all propellers have mixed and we can use a Gaussian profile. Here L is the vehicle size, which is twice the arm length. For the scope of this paper, we shall only deal with ZEF.

Based on experimental data, we choose an inverse decay model for the centerline velocity [12], [13].

$$\mathrm{V_{max}}(z) = \sqrt{\frac{T}{2\rho A_p}} \frac{\mathrm{c_{ax}} L}{(z - z_0)} \tag{1}$$

where $\sqrt{\frac{T}{2\rho A_p}}$ represents the induced velocity ($\mathrm{V_i}$) in the propeller plane given by momentum theory [14], T is the thrust produced by the propeller, ρ is the density of air, A_p is the propeller disk area, and z_0 is the virtual origin.

We normalize z with L for better intuition of velocity decay in terms of the vehicle size. The axial constant, $\mathrm{c_{ax}}$ is dimensionless and derived through experiments. Note that $\mathrm{c_{ax}}$ and z_0 depend on vehicle size and geometry according to our experimental data.

At any particular axial separation in ZEF, the velocity field follows a Gaussian profile with respect to radial separation [9], [10] given by,

$$V(z, r) = \mathrm{V_{max}}(z) \exp\left(-\mathrm{c_{rad}} \left(\frac{r}{z - z_0}\right)^2\right) \tag{2}$$

where $\mathrm{c_{rad}}$ is the radial decay rate and is dimensionless. It is derived using experimental data.

Since multirotor downwash is a free shear flow, the spread of the flow is assumed to grow linearly with axial separation [12], [15]. This explains the $(z - z_0)^2$ term in equation (2).

B. Drag

The force and torque due to drag is calculated using the velocity field from equation (2). We make the following assumptions about a multirotor frame:

1) It is a bluff body with a projected area onto a plane normal to the oncoming flow. This projected area is given by its CAD model
2) It has aerodynamic properties equivalent to a flat plate, with $C_D = 1.18$ [14].

We can predict drag force on one multirotor (large quadcopter) which is at a vertical separation of z below the other multirotor (small quadcopter) and horizontal separation of r. We assume that both the vehicles are hovering with zero roll and pitch angles. This gives us the drag force,

$$\boldsymbol{F}_D(z, r) = \int_{A_q} (-\boldsymbol{z}_{B,m}) \frac{1}{2} C_D \rho V^2(z', r') dA \tag{3}$$

where z' and r' are coordinates of points on the multirotor frame's surface, and A_q is the area of the multirotor frame.

The drag force integral can be calculated by dividing the multirotor frame's area into small elements and summing the forces on all these elements.

In a similar manner, we can predict torques using the velocity field as follows,

$$\boldsymbol{T}_D(z, r) = \int_{A_q} (\mathbf{r}' - \mathbf{r}) \times (-\boldsymbol{z}_{B,m}) \frac{1}{2} C_D \rho V^2(z', r') dA \tag{4}$$

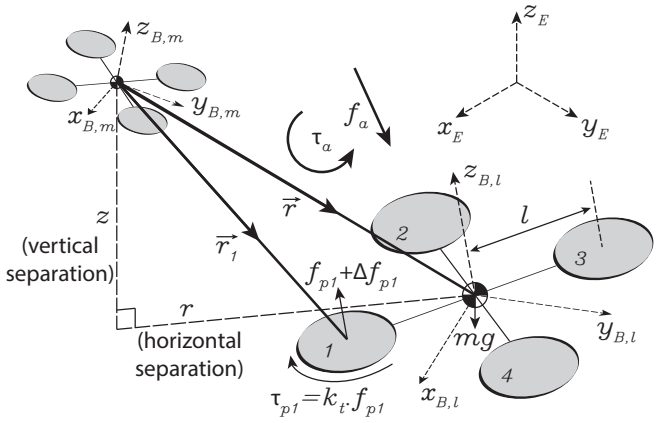

Fig. 2: Two quadcopters in proximity flight; body and inertial coordinate frames; forces and torques on large quadcopter

where $\mathbf{r}$ is the position vector of the center of mass of the multirotor, and $\mathbf{r}'$ is the position vector of some point on the multirotor's frame's surface.

We define the roll, pitch, and yaw torques as the torque about $\boldsymbol{x}_B, \boldsymbol{y}_B$, and $\boldsymbol{z}_B$ respectively. If both vehicles are hovering then their $\boldsymbol{z}_B$'s are aligned with $\boldsymbol{z}_E$ which leads to $(\mathbf{r}' - \mathbf{r})$ being in the x-y plane. This results in the torque due to drag also being in the x-y plane, which implies that the yaw torque would be zero.

C. Change in Propeller Thrusts

Momentum theory [14] indicates that thrust produced by a propeller decreases as oncoming flow incident on the plane of the propeller increases in velocity, subject to constant power consumption. This effect has been addressed in [16] which compares hover thrusts with and without oncoming flows and approximates the effect as a fourth order polynomial in oncoming flow velocity, and in [17] which uses blade element momentum theory. alysis, we make the following assumptions: all oncoming flows are normal to the plane of the propeller, and Δf_p is a function of propeller speed (ω_p) and oncoming flow velocity $(\mathrm{v_{on}})$. We know that the thrust is proportional to the square of propeller speed [14]. We denote the original propeller force as $f_{p,old} = \mathrm{k_1}\omega_p^2$, and the propeller force with oncoming flow as $f_{p,new} = \mathrm{k_2(v_{on})}\omega_p^2$.

Clearly, $\mathrm{k_2}(0) = \mathrm{k_1}$. We make a first order approximation for $\mathrm{k_2(v_{on})}$ given by,

$$\mathrm{k_2(v_{on})} = \mathrm{k_1} - \mathrm{b_v v_{on}} \tag{5}$$

where $\mathrm{b_v}$ is the thrust decay coefficient, which is obtained experimentally.

Using equation (5), and $\Delta f_{pi} = f_{p,new} - f_{p,old}$, the change in propeller thrust is given by,

$$\Delta f_{pi}\left(\omega_{pi}, \mathrm{v_{on}}\right) = -\mathrm{b_v v_{on}}\omega_{pi}^2 \tag{6}$$

In the case of one vehicle flying below another, the oncoming flow velocity experienced by the bottom vehicle is a function of its relative separation from the top vehicle. In general, each propeller of the bottom vehicle will experience a different oncoming flow velocity. Let the propellers, numbered $i = 1$ through n, be at position (z_i, r_i).

The total disturbance force that the multirotor experiences due to change in propeller thrusts is the sum of Δf_{pi} of each propeller, which are assumed to be parallel to the vehicle's z-axis, $\boldsymbol{z}_B$. The disturbance force due to change in propeller forces is then given by,

$$\boldsymbol{F}_P = \sum_{i=1}^{n} \boldsymbol{z}_B \Delta f_{pi}\left(\omega_{pi}, \mathrm{v_{on}}(z_i, r_i)\right) \tag{7}$$

The Δf_{pi} for each propeller may be different, which produces a net torque on the vehicle. If the position vector of a propeller is $\mathbf{r}_i$, then torque due to Δf_p is given by,

$$\boldsymbol{T}_P = \sum_{i=1}^{n} (\mathbf{r}_i - \mathbf{r}) \times (\boldsymbol{z}_B) \Delta f_{pi} \tag{8}$$

Combining the effects of drag and change in propeller thrust, we can predict the aerodynamic force and torque at any relative separation. This completes the model for estimating aerodynamic disturbances.

III. Disturbance Characterization

In this section, we present the derivation of equations on how to obtain aerodynamic forces and torques using data from an accelerometer, rate-gyro, and propeller forces.

A. Force disturbance equations

The output of accelerometer $(\boldsymbol{\alpha})$ is related to linear acceleration of the body $(\boldsymbol{a})$ as,

$$\boldsymbol{R\alpha} = \boldsymbol{a} - \boldsymbol{g} \tag{9}$$

where $\boldsymbol{g}$ is the acceleration due to gravity, and $\boldsymbol{R}$ is a rotation matrix which converts body frame vectors to the inertial frame. The rotation matrix is obtained via the roll, pitch and yaw angles of the quadcopter.

Application of Newton's second law to the large quadcopter shown in Figure 2 yields,

$$m\boldsymbol{a} = \boldsymbol{f}_p + \boldsymbol{f}_a + m\boldsymbol{g} \tag{10}$$

where m is the mass of the body, $\boldsymbol{f}_a$ is the aerodynamic force, and $\boldsymbol{f}_p$ is the total propeller force.

Combining equations (9) and (10), we get,

$$\boldsymbol{f}_a = m\boldsymbol{R\alpha} - \sum_{i=1}^{4} f_{pi}\boldsymbol{z}_B \tag{11}$$

We have access to f_{pi}'s from the input PWM signal and a-priori propeller calibration data. We also have data of position and orientation of each quadcopter from the motion-capture system, which can be used to calculate relative horizontal and vertical separations between the vehicles. Thus, we can estimate aerodynamic forces as a function of relative separation between the quadcopters.

B. Torque disturbance equations

The onboard rate-gyro gives us angular velocity. This can be differentiated using the forward Euler method to estimate angular acceleration as follows,

$$\dot{\boldsymbol{\omega}}_k = \frac{\boldsymbol{\omega}_{k+1} - \boldsymbol{\omega}_k}{t_{k+1} - t_k} \tag{12}$$

Applying Newton's second law for rotation to the large quadcopter, we can write,

$$\boldsymbol{R}\boldsymbol{J}\dot{\boldsymbol{\omega}} = \boldsymbol{R}\boldsymbol{\tau}_p + \boldsymbol{\tau}_a \tag{13}$$

Here, $\boldsymbol{J}$ is the mass moment of inertia tensor of the body, $\boldsymbol{\tau}_a$ is the aerodynamic torque in the inertial frame, $\boldsymbol{\tau}_p$ is torque due to propeller forces in the body frame, and $\boldsymbol{\omega}$ and $\dot{\boldsymbol{\omega}}$ are the angular velocity and angular acceleration of the body in the body frame.

The torque due to propellers is a result of differences in propeller forces which create a moment about the center of the quadcopter. Referring to Figure 2, we get,

$$\tau_{px} = \frac{l}{\sqrt{2}}[(f_{p3} + f_{p4}) - (f_{p1} + f_{p2})] \tag{14a}$$

$$\tau_{py} = \frac{l}{\sqrt{2}}[(f_{p2} + f_{p3}) - (f_{p1} + f_{p4})] \tag{14b}$$

$$\tau_{pz} = \mathrm{k_t}[(f_{p2} + f_{p4}) - (f_{p1} + f_{p3})] \tag{14c}$$

where $\mathrm{k_t}$ is the torque to thrust ratio of a propeller, which is obtained experimentally using an RC Benchmark Series 1580 thrust stand.

IV. Validation

In this section, we present our laboratory setup, derivation of empirical parameters, experiments that we conduct, model predictions, experimental results, a comparison between the two, and a discussion on the same.

A. Laboratory setup

We have introduced the two types of quadcopters that we use for our experiments in section I. The vehicles are localized via sensor fusion of a motion-capture system and an onboard inertial measurement unit. Experimental data from the accelerometer, rate gyroscope, motion-capture system, and propeller forces are logged for post-processing.

B. Velocity field model parameters

We determine the fit parameters $(\mathrm{c_{ax}}, z_0, \mathrm{c_{rad}})$ by measuring velocities at various separations in the downwash of the quadcopters. Figure 3 shows a schematic of our flow velocity measurement experiment. We mount the quadcopter sideways, such that its thrust axis is horizontal. It is ensured that the quadcopter mount and all our measurements points are far away ($> 1.0\,\mathrm{m}$) from walls so that the flow field is unaffected by those. Velocity is measured using a constant temperature anemometer (TSI Inc. model 1212-60).

Figure 6 (top-left) shows the centerline velocities for the small quadcopter downwash. A least-squares fit is used over the data, with z_0 and $\mathrm{c_{ax}}$ as the variables. We get $\mathrm{c_{ax}} = 4.672$, and $z_0 = 0.033\,\mathrm{m}$.

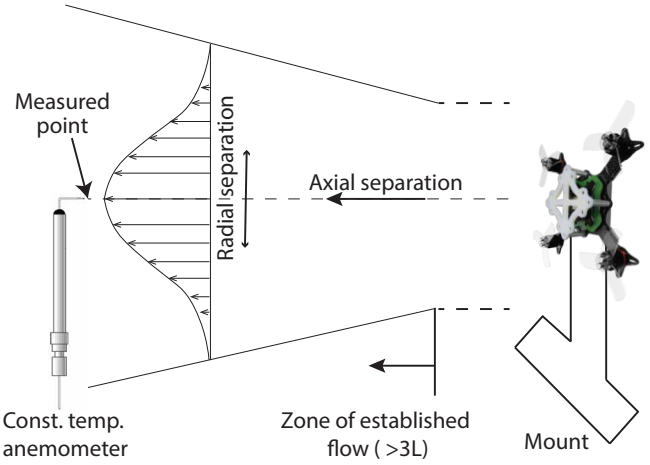

Fig. 3: Flow velocity measurement schematic

Figure 6 (bottom-left) shows the velocities measured for the small quadcopter but with an axial and radial separation. A least-squares fit is used over the data with $\mathrm{c_{rad}}$ as the variable, which gives us $\mathrm{c_{rad}} = 60.808$.

The same velocity model is also used for the large quadcopter's downwash data. The plots for centerline velocities, and velocities with radial and axial separations are shown in Figure 6 (right). The respective parameters from least-squares fit for large quadcopter's downwash are $\mathrm{c_{ax}} = 4.886$, $z_0 = 0.110\,\mathrm{m}$, and $\mathrm{c_{rad}} = 24.936$. Note that we do not take the first point ($z = 1.59L$) of large quadcopter's centerline velocity data for the fit because it does not lie in the ZEF. A low velocity is measured at this point, which is also shown in literature experimentally [7][18] and numerically [19].

For axisymmetric, turbulent jet, reported values of $\mathrm{c_{ax}}$ in [13] matched well with derived values. Location of virtual origin depends on the initial flow profile [20], and the value can be either positive (downstream) or negative (upstream) [13][21].

Although the values of fit parameters are not same for the vehicles, these values are consistent across multiple thrust values for each vehicle. This suggests that the fit parameters are dependent on vehicle geometry and the properties of the fluid we are operating in.

C. Propeller thrust change characterization

We experimentally characterize the propeller thrust changes as a function of ω_p and $\mathrm{v_{on}}$. We use a nozzle with an industrial fan attached to its inlet, and a honeycomb mesh in front of the fan to produce a uniform flow at the exit of the nozzle. The industrial fan has a controllable speed setting allowing us to vary the velocity of flow incident on the propeller. We measure the thrust produced by the propeller for various propeller speeds and oncoming flow velocities using a thrust stand. The thrust decay coefficient is calculated via a least-squares fit, and we obtain a value of $\mathrm{b_v} = 3.710 \times 10^{-7}\,\mathrm{Nm^{-1}rad^{-2}s^3}$.

D. Controller

For our vehicles, we use a cascaded PID position and attitude controller shown in Figure 4. The integral term in the controller for the position and yaw allows us to achieve zero steady-state error. The position controller ensures that roll and pitch do not have a steady-state error.

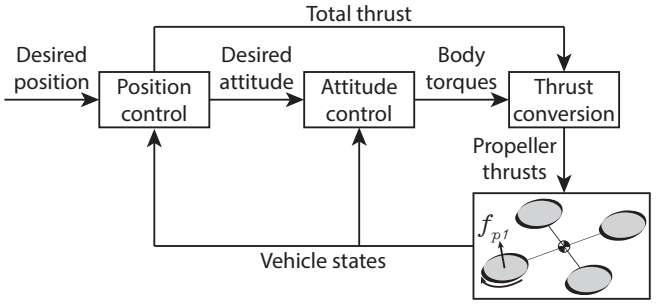

Fig. 4: Block diagram of the controller

E. Experiment description

We perform constant velocity sweep experiments to characterize aerodynamic disturbances. In these experiments, one of the vehicles is commanded to maintain a position setpoint, and the other vehicle moves from one position setpoint to another at a constant velocity. The velocity is kept low enough so that the motion of the vehicle does not affect our characterization. We present results from horizontal sweep experiments.

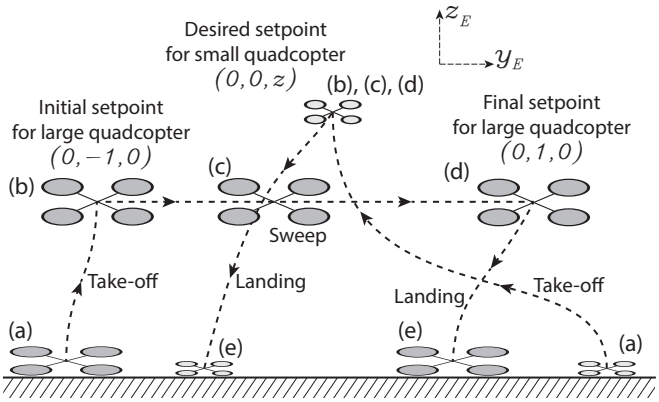

Fig. 5: Illustration of a horizontal sweep experiment: (a) Quadcopters take-off, (b) small quadcopter reaches its desired setpoint, large quadcopter reaches the initial setpoint, (c) large quadcopter begins the constant velocity sweep in +y-direction, (d) large quadcopter reaches the final setpoint, (e) Quadcopters land

F. Model predictions

The predictions that we present are for horizontal sweep experiments where the small quadcopter maintains a fixed setpoint $(0, 0, z)$ and the large quadcopter is flown below the small quadcopter from $(0, -1, 0)$ to $(0, 1, 0)$, shown in Figure 5. We perform these experiments for $z \in \{0.5, 1.0, 1.5, 2.0, 2.5\}$ m. Figure 7 presents the plots for aerodynamic disturbance force in z-direction (left) and roll torque (right) on the large quadcopter versus the Y-coordinate of the large quadcopter due to downwash of the small quadcopter. Top plots show the effect due to aerodynamic drag and bottom plots due to change in propeller thrusts. The combined effect of the two mechanisms is shown in Figure 8. Forces on the large quadcopter are symmetrically distributed about $\boldsymbol{y}_B$ which results in zero pitch torque.

G. Experimental results

Figure 8 shows plot of aerodynamic force in z-direction (left) and roll torque (right) on the large quadcopter obtained via experiments. They have been plotted along with predictions from the model for comparison. The accelerometer and rate-gyro readings contain noise in the raw format and we smooth that data using a moving average with a triangular window function, which helps in visualization of the data.

H. Comparison and discussion of results

We make the following observations about predictions from the model:

1) For vertical separations greater than one meter, the disturbances due to change in propeller thrusts are much higher in magnitude as compared to those due to aerodynamic drag.

2) The forces and torques start from zero at high values of r, which is expected because the downwash velocities are very low in this region. As the large quadcopter moves closer to $r = 0$, the magnitude of forces starts to increase and achieves a maximum at $r = 0$. On the other hand, the torques attain a maximum at some non-zero r and go to zero at $r = 0$. This is expected because at $r = 0$, the forces on the quadcopter are distributed symmetrically.

3) Both the magnitude and the spread of the velocity field affect the forces and torques. For example, we know that centerline flow velocity is higher for lower z, that is when the two vehicles are closer. So for our experiments, we have highest centerline velocity for $z = 0.5\,\mathrm{m}$, but Figure 7 shows that force due to change in propeller thrust is lower for $z = 0.5$ as compared the force at higher z values. This is because the velocity field is narrow at $z = 0.5$ compared to the field at greater axial separations. Consequently, the propeller area affected by the oncoming flow at $z = 0.5$ is lower as compared to the affected area for higher z values. The force due to change in propeller thrust is thus small at very low axial separations.

4) The spread of the forces and torques due to drag and change in thrusts increases monotonically with increasing z. However, the peak magnitude of these forces and torques is not monotonic with respect to z. It attains a maximum value and then starts decaying. This happens as a result of increasing spread but decreasing centerline velocity, with increasing z.

We make the following observations about experimentally derived disturbances:

1) The forces and torques follow a similar trend as the predicted values. They start from zero at high values of r. As the large quadcopter moves closer to $r = 0$, the magnitude of force starts to increase and achieves a maximum at $r = 0$.

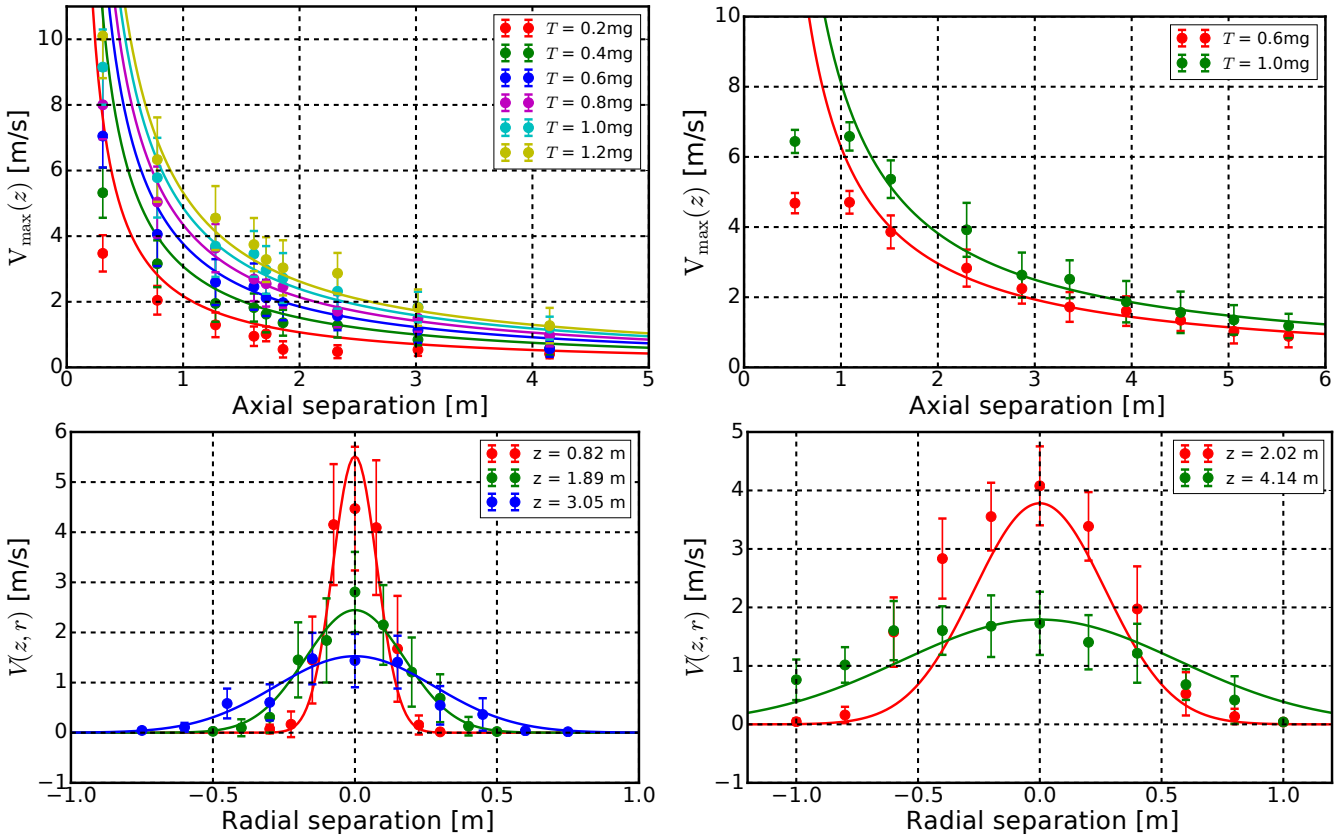

Fig. 6: Centerline flow velocity vs. axial separation for various thrusts (top), and axial flow velocity vs. radial separation for various axial separations (bottom). Presented data for small quadcopter (left) and large quadcopter (right). Error bars represent standard deviation of time-series data.

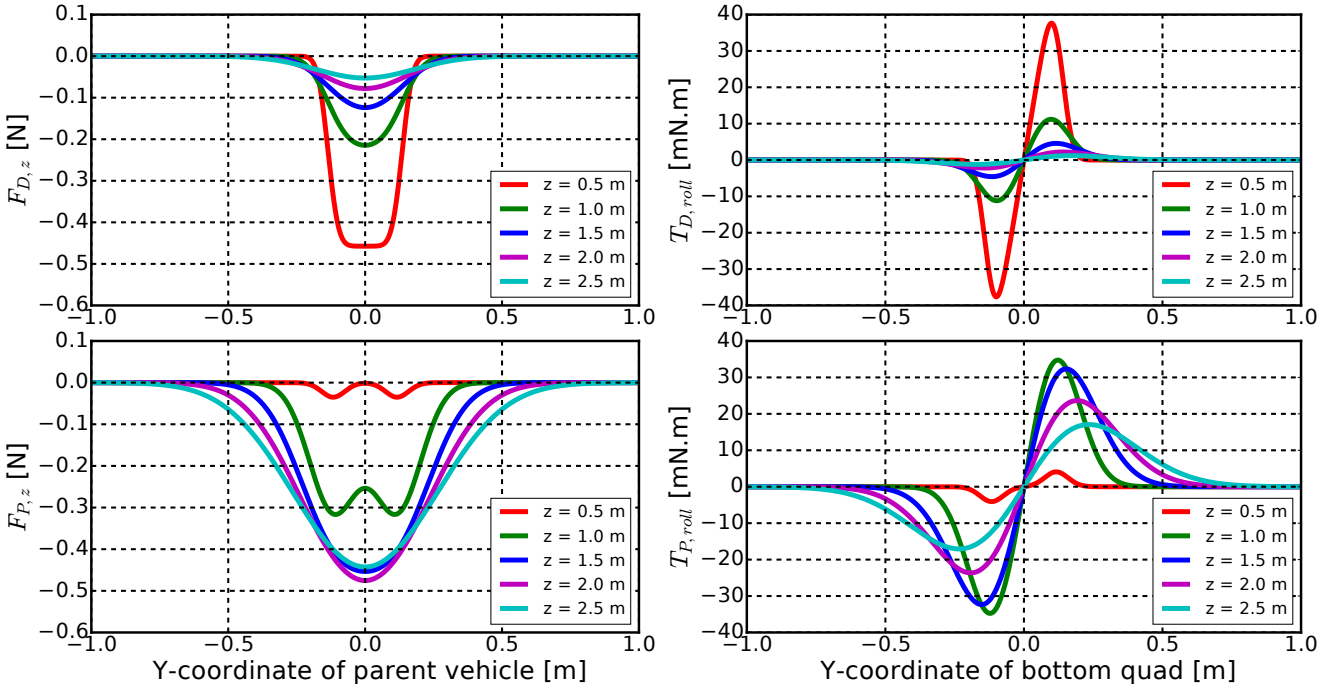

Fig. 7: Predicted values of aerodynamic forces in z-direction (left) and roll torques (right) due to drag (top) and change in propeller thrust (bottom)

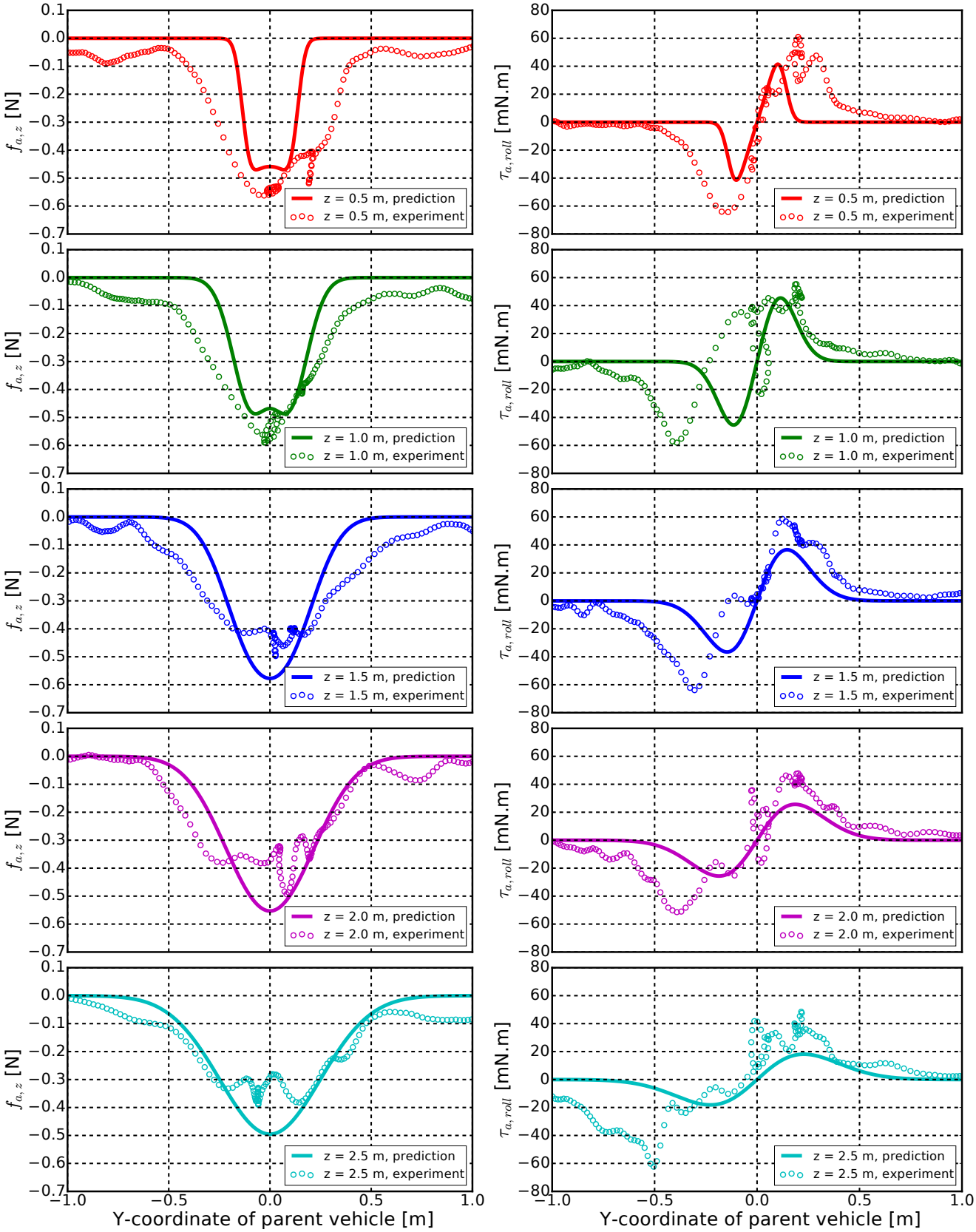

Fig. 8: Aerodynamic forces in z-direction (left) and roll torques (right). Solid lines show predicted values due to combined effect of drag and change in propeller thrust. Scatter plots show experimentally derived values.

The torques attain a maximum at some non-zero r and go to zero near $r = 0$.

2) The values near $r = 0$ fluctuate a lot. This happens during the experiment because the large quadcopter is trying to counter the aerodynamic disturbances, which leads to some oscillations in position and attitude.

3) The forces on small quadcopter for the horizontal sweep experiments were less than 3% of its weight. On the large quadcopter, these were about 10% of the large quadcopter's weight. We can conclude that the disturbance effect due to airflow is much less pronounced on the vehicle that flies higher.

We now compare the results from our experiments with predictions from the model:

1) The predicted and experimentally derived forces and torques match well both in magnitude and spread for larger values of vertical separations, $z \in \{1.0, 1.5, 2.0, 2.5\}\mathrm{m}$. However, the model fails to predict the disturbances well for lower vertical separations such as $z = 0.5\,\mathrm{m}$. This can be attributed to the fact that our velocity field model assumes the flow to start from a virtual downstream point, and spreads linearly with axial separation. In reality, we have a quadcopter which is not producing flow through a point, but via four propellers placed certain distances apart. In the near field, $z \leq 6L$ [13], this flow field initially contracts due to acceleration from propellers and then expands due to deceleration from viscous effects. This is not captured by our velocity model, which leads to discrepancy between the predictions and experiments for low values of z.

2) Both the experiments and predictions show that there is a cutoff horizontal separation beyond which the disturbance on the large quadcopter is negligible. This cutoff separation is dependent on the vehicle sizes, and the vertical separation. This information can be used to plan a trajectory for a docking maneuver or to minimize the disturbance effect from other vehicles' airflow.

3) We have observed that major component of the forces and torques are due to change in propeller thrusts rather than aerodynamic drag. So for predicting disturbances with higher accuracy, we need to characterize the propeller thrust changes with higher accuracy and precision.

4) We have a good match between predictions and experiments for $z > 1.0\,\mathrm{m}$. This information can be exploited to compensate for the disturbance effect by incorporating it into the control algorithm for improved stability during a proximity flight maneuver.

V. Conclusions and Future Work

In this paper, we have explored the disturbance effect of airflow of one quadcopter on another in terms of the aerodynamic forces and torques that the other quadcopter experiences. We have built a model for the velocity field below a multirotor by employing an inverse decay model for the center-line velocity along with a Gaussian distribution of velocities with respect to radial separation. This model was based on a combination of existing literature and experimental flow data measured for our quadcopters.

We then developed a model to theoretically characterize the aerodynamic forces and torques. This was based on the assumption that these disturbances are mainly caused by two mechanisms: aerodynamic drag and change in propeller thrust due to oncoming flow.

We have derived equations to characterize the aerodynamic disturbances using data from sensors, specifically accelerometer and rate-gyro. We have then flown two quadcopters simultaneously and characterized these disturbances with respect to relative separation.

We finally compared the predictions of forces and torques from the model with those obtained experimentally and verified that the model predicts the forces and torques well for certain ranges of relative separation, especially when vertical separation is more than a meter. This information can be used by a multirotor, for example, to compensate for disturbances due to airflow when flying in the downwash of another multirotor, which most of the current applications choose to avoid.

In future work, we will improve the velocity model at lower vertical separations by incorporating the effect of a multirotor's size on the spread of velocity for better predictions of forces and torques in that region. Results from the model and experiments may be used to develop a controller that can compensate the aerodynamic disturbances and plan intelligent trajectories for multirotors flying in close formations such that they are minimally affected. We can then utilize the compensating controller and trajectories for applications such as package transfers, co-operative lifting of a heavy payload using multiple multirotors, or docking.

Acknowledgment

We acknowledge financial support from NAVER LABS. The experimental testbed at the HiPeRLab is the result of contributions of many people, a full list of which can be found at `hiperlab.berkeley.edu/members/`.

The authors wish to acknowledge Christian Castaneda Cuella for helping with manufacturing of the nozzle used in characterization of propeller thrusts with oncoming flow.

References

[1] F. Augugliaro, S. Lupashin, M. Hamer, C. Male, M. Hehn, M. W. Mueller, J. S. Willmann, F. Gramazio, M. Kohler, and R. D'Andrea, "The flight assembled architecture installation: Cooperative construction with flying machines," *IEEE Control Systems Magazine*, vol. 34, no. 4, pp. 46–64, 2014.

[2] A. Mirjan, F. Augugliaro, R. DAndrea, F. Gramazio, and M. Kohler, "Building a bridge with flying robots," in *Robotic Fabrication in Architecture, Art and Design 2016*. Springer, 2016, pp. 34–47.

[3] A. Khan, B. Rinner, and A. Cavallaro, "Cooperative robots to observe moving targets: Review," *IEEE Transactions on Cybernetics*, vol. 48, no. 1, pp. 187–198, 2018.

[4] S. Reynaud, M. Kieffer, H. Piet-Lahanier, and L. Reboul, "A set-membership approach to find and track multiple targets using a fleet of uavs," in *2018 IEEE Conference on Decision and Control (CDC)*. IEEE, 2018, pp. 484–489.

[5] I. Sharf, M. Nahon, A. Harmat, W. Khan, M. Michini, N. Speal, M. Trentini, T. Tsadok, and T. Wang, "Ground effect experiments and model validation with draganflyer x8 rotorcraft," in *2014 International Conference on Unmanned Aircraft Systems (ICUAS)*. IEEE, 2014, pp. 1158–1166.

[6] P. Sanchez-Cuevas, G. Heredia, and A. Ollero, "Multirotor uas for bridge inspection by contact using the ceiling effect," in *2017 International Conference on Unmanned Aircraft Systems (ICUAS)*. IEEE, 2017, pp. 767–774.

[7] R. Miyazaki, R. Jiang, H. Paul, K. Ono, and K. Shimonomura, "Airborne docking for multi-rotor aerial manipulations," *IEEE/RSJ International Conference on Intelligent Robots and Systems (IROS)*, 2018.

[8] W. Hönig, J. A. Preiss, T. S. Kumar, G. S. Sukhatme, and N. Ayanian, "Trajectory planning for quadrotor swarms," *IEEE Transactions on Robotics*, vol. 34, no. 4, pp. 856–869, 2018.

[9] D. Yeo1, E. Shrestha, D. A. Paley, and E. Atkins, "An empirical model of rotorcraft uav downwash for disturbance localization and avoidance," *AIAA SciTech Forum*, 2015.

[10] W. Khan, R. Caverly, and M. Nahon, "Propeller slipstream model for small unmanned aerial vehicles," *AIAA Modeling and Simulation Technologies (MST) Conference*, 2013.

[11] E. Hirst, "Analysis of buoyant jets within the zone of flow establishment." Oak Ridge National Lab., Tenn., Tech. Rep., 1971.

[12] S. B. Pope and S. B. Pope, *Turbulent flows*. Cambridge university press, 2000.

[13] H. Fellouah, C. Ball, and A. Pollard, "Reynolds number effects within the development region of a turbulent round free jet," *International Journal of Heat and Mass Transfer*, vol. 52, no. 17-18, pp. 3943–3954, 2009.

[14] B. McCormick, "Aerodynamics aeronautics and flight mechanics," 1995.

[15] P. Davidson, *Turbulence: an introduction for scientists and engineers*. Oxford University Press, 2015.

[16] G. M. Hoffmann, H. Huang, S. L. Waslander, and C. J. Tomlin, "Quadrotor helicopter flight dynamics and control: Theory and experiment," *AIAA Guidance, Navigation and Control Conference and Exhibit*, 2007.

[17] M. Bangura and R. Mahony, "Thrust control for multirotor aerial vehicles," *IEEE Transactions on Robotics*, vol. 33, no. 2, pp. 390–405, 2017.

[18] D. Shukla and N. Komerath, "Multirotor drone aerodynamic interaction investigation," *Drones*, vol. 2, no. 4, 2018. [Online]. Available: http://www.mdpi.com/2504-446X/2/4/43

[19] S. Yoon, H. C. Lee, and T. H. Pulliam, "Computational analysis of multi-rotor flows," in *54th AIAA Aerospace Sciences Meeting*, 2016, p. 0812.

[20] M. Uddin and A. Pollard, "Self-similarity of coflowing jets: the virtual origin," *Physics of fluids*, vol. 19, no. 6, p. 068103, 2007.

[21] N. E. Kotsovinos, "A note on the spreading rate and virtual origin of a plane turbulent jet," *Journal of Fluid Mechanics*, vol. 77, no. 2, pp. 305–311, 1976.